Computational Condensed Matter 40 (2024) e00950

Contents lists available at ScienceDirect

Computational Condensed Matter

journal homepage: www.elsevier.com/locate/cocom

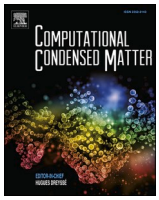

Investigation of direct small bandgap Cs_2AuInX_6 (X= F/Cl) double perovskites for energy harvesting technology employing DFT

S. Mahmud [a,*], M.A.U.Z. Atik [b], M.N. Mostakim [b], Md. Tarekuzzaman [c], Md. Zahid Hasan [c]

[a] Department of Electrical and Electronic Engineering, Jatiya Kabi Kazi Nazul Islam University (JKKNIU), Mymensingh, 2224, Bangladesh
[b] Department of Electrical and Electronic Engineering, Atish Dipankar University of Science and Technology (ADUST), Dhaka, 1230, Bangladesh
[c] Department of Electrical and Electronic Engineering, International Islamic University Chittagong, Kumira, Chittagong, 4318, Bangladesh

ARTICLE INFO

Keywords:
Double perovskite
DFT
Direct band gap
Lattice thermal conductivity
Figure of merit

ABSTRACT

In this work, the ground-state structures of the double perovskite material Cs_2AuInX_6 (X = F/Cl) are determined using density functional theory (DFT) in the context of energy harvesting technology. The octahedral and tolerance factors demonstrate structural stability, indicating that the compound is cubic. The material Cs_2AuInX_6 (X = F/Cl) under study has its dynamic stability confirmed by formation energy and binding energy, and its thermodynamic stability checkeded by phonon dispersion. Mechanical stability is verified by Pugh's ratio (>1.75), Poison's ratio (>0.26), and Cauchy's pressure (>0), which show the ductile behavior of the studied Cs_2AuInX_6 (X = F/Cl) compounds. The direct band gaps, determined via TB-mBJ, are 0.51 eV and 0.29 eV for Cs_2AuInF_6 and $Cs_2AuInCl_6$, respectively. Furthermore, their low effective mass suggests excellent carrier mobility. The optical constants, such as dielectric constants, refractive index, absorption coefficient, and optical reflectivity, are also calculated to shed more light on their electronic nature. The absorption coefficients of the materials are 3.21×10^5 and 2.24×10^5 cm^{-1} for the titled materials, respectively. The investigated compounds, Cs_2AuInX_6 (X = F/Cl), have actual figures of merit of 0.43 and 0.42 at 300 K, respectively, which can lead to energy-collecting applications such as clean energy technology.

1. Introduction

The growth of contemporary technology has led to an enhancement in the human quality of life, resulting in worldwide economic development. Consequently, the researchers' endeavors to discover alternative energy sources to fossil fuels and other traditional sources have intensified due to the significant rise in energy demand. Present-day energy sources pose significant risks to the environment and are rapidly diminishing [1,2]. Hence, a wide range of renewable energy sources are currently undergoing extensive research as potential substitutes for the current energy sources [3–5].

Double perovskite materials are becoming popular for various energy harvesting applications because of their unique blend of mechanical, structural, thermoelectric, and optoelectronic properties. The structural stability of energy-collecting equipment is critical to determining its long-term performance. Double-perovskite materials achieved longer device lifetimes with higher structural stability, which lowers the chance of deterioration over time. Mechanical stability is another important consideration since mechanical stress is common in energy-collecting systems. Double perovskite materials with high mechanical stability can withstand the rigors of practical applications and can withstand more damage. To develop renewable energy devices, a material's optoelectronic and thermoelectric properties must be explored. Materials with a direct bandgap are appropriate for optoelectronic uses [6,7].

Thermoelectric properties are necessary to harvest thermoelectric energy and convert heat into electricity, increasing thermoelectric performance [8]. Due to their ability to generate a significant amount of electricity from waste heat, double-perovskite materials are a promising method for sustainable energy production. Materials with a small bandgap are highly suitable for thermoelectric applications [9]. The general formula for these materials is $A_2BB'X_6$, where A and B are cations and X is an anion. The A-site cations often occupy the bigger cavities in the perovskite structure, whereas the B-site cations and X-site anions typically fill the smaller ones. The special properties of double perovskite materials can be altered by modifying the material's composition. They display a wide variety of compositions, which can be used in vast applications.

* Corresponding author.
E-mail address: shuaib.eee.iu@gmail.com (S. Mahmud).

https://doi.org/10.1016/j.cocom.2024.e00950
Received 16 May 2024; Received in revised form 4 August 2024; Accepted 5 August 2024
Available online 6 August 2024

A variety of research studies have been conducted globally due to the highly promising features exhibited by halide double perovskites [10–19]. Halide double perovskites have recently garnered a lot of attention for use in optoelectronic devices because of their direct and small band gaps [20]. Comparably, Noor et al.'s [21] study of the double perovskite halides A_2ScInI_6 (A = Rb, Cs) used the density-functional theory (DFT) to uncover a small and direct band gap, indicating that halides are best suited for use in optoelectronic devices and that their best absorption of light occurs in infrared (IR) regions. Another study by Aslam et al. [22] examined the electrical, optical, and thermoelectric characteristics of the Bi-based double perovskites halides, Cs_2InBiX_6 (X = Cl, Br, and I), using the DFT method. The compound is suitable for application in solar-absorbing devices and energy conversion because of its predicted thermoelectric and optical properties, which indicate a small and direct band gap. Comparable studies in Refs. [23,24], showed enhanced stability and a direct band gap between 1.5 and 3 eV. Their high absorption coefficient makes them attractive for use in solar cell applications as well. DFT is used by S. Iqbal et al. [25] to study the structural, optoelectronic, and thermoelectric properties of halide-based double perovskite Rb_2AlInX_6 (Cl, Br, and I) compounds, which have narrow and indirect bandgaps (1.05, 0.65, and 0.25 eV) and are potential optoelectronic devices. Similarly, N. P. Mathew et al. [26] show that due to the direct small band gap (1.1 eV) and high optical absorption in the visible range, the compound $Cs_2AgInCl_6$ might be a strong candidate for potential applications in opto-electronics and photovoltaics, making it more prospective for the absorber layer in solar cells. To summarize the aforementioned literature, the researchers primarily concentrate on the structural, mechanical, electrical, optical, and thermoelectric characteristics of the DPs.

In the current work, we have explored the stability, optical, electronic, and thermo-electric properties of double perovskites Cs_2AuInX_6 (X = F/Cl) with Wien2K and BoltzTraP2 codes. The optical properties, such as the real and imaginary parts of the dielectric constant, refractive index, absorption coefficient, and optical reflectivity of the studied compound, are also measured by calculating their dielectric functions. These analyses will yield useful insights for researchers, facilitating the future commercialization of the studied compounds. Their excellent structural stability, together with their direct and small band gap, improves their performance for solar cells and IR photodetectors.

2. Computational technique

This work carried out the first principle calculations by the Wien2k code, which is based on the FP-LAPW method [27]. The code employs an iteration process to determine the compound's electronic ground state. The SCF cycle requires iteratively solving the Kohn-Sham equations until it achieves self-consistency. The GGA-PBE [28] performed the structural optimization to obtain an accurate lattice parameter and bulk modulus. For this, the input parameters were set as: charge convergence 10^{-4}e, energy convergence 10^{-5} Ry, product of muffin tin radius, R_{MT} and plane wave vector, K_{max}, is 8; Fourier expansion maximum charge density, $G_{max} = 12$, and 1000 ($10 \times 10 \times 10$) k points. By applying the IRelast package [29] included in wien2k, the elastic characteristics of the materials have been computed in order to verify the mechanical stability of the material being studied. To compute the electrical, optical, and thermal characteristics, a denser k-mesh of 10,000 was used. Additionally, since the TB-mBJ [30] technique matches the experimental result and is time-efficient, it was employed to compute the correct band gap. By incorporating the relaxation period, the Boltztrap2 [31] method was used to describe the thermoelectric behavior. The finite displacement approach was used to calculate the material's dynamical stability.

3. Results and discussion

3.1. Structural properties and stability

The double perovskite crystal structure of Cs_2AuInX_6 is derived from the formula of $A_2BB'X_6$, which is represented by a three-dimensional network of shared-corner octahedra as depicted in Fig. 1. Each Au and In ion is paired with a $6Cl^-$ ion, while every Cs^+ ion is linked with a $12Cl^-$ ion. Double perovskites show special structural characteristics and stability because they have a large A-site cation and two distinct cations at the B-site. The least amount of energy that corresponds to the minimum volume is observed in order to compute lattice constants. The lattice parameters calculated for Cs_2AuInX_6 are given in Table 1. The Birch-Murnaghan equation of state [32], which is integrated with the ground state's cubic structural stability. The optimized bulk modulus (B) for the Cs_2AuInX_6 material, which is also provided in Table 1, illustrates the stiffness and compressibility of these compounds. The structural stability of Cs_2AuInX_6 is analyzed using Goldschmidt's tolerance factor, t_G and octahedral factor, μ [33], which are provided below:

$$t_G = \frac{r_A + r_X}{\sqrt{2}(r_B + r_X)}; \quad \mu = \frac{r_B}{r_X}$$

In the formula for tolerance factor, the atomic radii of Cs and, halogen (X) atoms are presented by r_A and r_X [34]. For double perovskite r_B is taken as the average of Au and In ionic radii. Thus, the iconic radii of each element are expressed by $r_A = 1.88$ Å for Cs, $r'_B = 1.37$ Å for Au, $r''_B = 0.8$ Å for In and = 1.33 Å, and 1.81 Å for F and Cl respectively [35]. The values of t_g and $\boldsymbol{\mu}$ are determined using Shanon's radii for the respected atoms in Cs_2AuInX_6. The ranges for tg and $\boldsymbol{\mu}$ should be $0.81 < t_G < 1.1$ and $0.41 < \boldsymbol{\mu} < 0.89$, respectively, for the perovskites to stay most stable. The calculated values are 0.93 (X = F) and 0.90 (X = Cl) for t_G, and 0.81 (X = F) and 0.59 (X = Cl) for $\boldsymbol{\mu}$, respectively, which are in accordance with the typical range of halide perovskite and also satisfactory for stable structures of these compounds. We can thus expect all compounds to crystallize in the cubic perovskite phase due to their suitable tolerance factors.

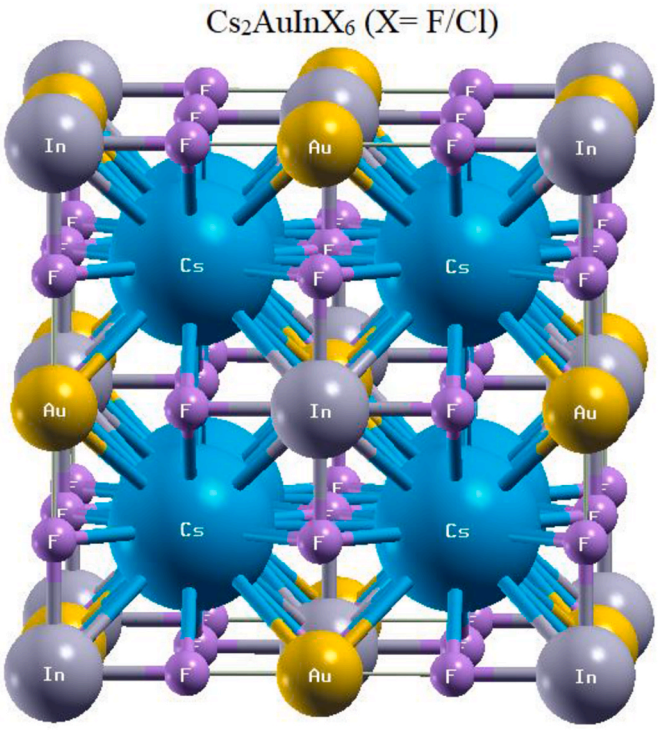

Fig. 1. Unit cell of Cs_2AuInX_6 (X = F/Cl).

Table 1
Physical entity of compounds.

Parameter	Cs_2AuInF_6	$Cs_2AuInCl_6$
Lattice constant, a=b=c (Å)	9.2169	10.6455
a=b=c (Bohr)	17.4175	20.1170
Unit cell volume, V ($Bohr^3$)	1320.98	2035.31
Tolerance factor, t_G	0.93	0.90
Octahedral factor, μ	0.81	0.59
Formation energy, E_F (eV/atom)	−3.13	−2.00
Binding energy, E_b (eV/atom)	−4.26	−3.51
Minimum Energy, E_0 (Ry)	−82222.83	−86562.51
Bulk modulus B_0	50.78	30.76
B_0'	3.62	1.24

The formation energy (E_f) and binding energy (E_b) of dynamically stable studied halide double perovskites are calculated using the following formula [36,37]:

$$E_f = \frac{E_{Total} - \left(n_{Cs} \times \frac{E_{Cs}}{p} + n_{Au} \times \frac{E_{Au}}{q} + n_{In} \times \frac{E_{In}}{r} + n_X \times \frac{E_X}{s}\right)}{N}$$

$$E_b = E_{Total} - (n_{Cs} \times \mu_{Cs} + n_{Au} \times \mu_{Au} + n_{In} \times \mu_{In} + n_X \times \mu_X)$$

It provides the energy difference (formation energy) between bulk Cs, Au, In and X element unit cells and Cs_2AuInX_6 (X = F/Cl) compounds. In this case, the energies and number of the atoms of Cs, Au, In, and X are denoted by E_{Cs}, E_{Au}, E_{In}, and E_X, and n_{Cs}, n_{Au}, n_{In}, n_X, respectively, while μ stands for individual state energy of the material. The number of atoms in each element is indicated by its coefficients, p, q, r, and s in E_{Cs}, E_{Au}, E_{In} and E_X. The entire energy released during the production of perovskites is indicated by the symbol E_{Total} (Cs_2AuInX_6). All of these calculated values are shown in Table 1, and their negative signs indicate that the substances under observation are dynamically stable [38]. It is also noteworthy that the compound Cs_2AuInF_6 has a greater negative value than $Cs_2AuInCl_6$ for both formation and binding enery, which indicates that the F-based composition is more stable.

It is important to note that compounds with larger negative formation and binding energies typically have more stable structures. In light of this, Table 1 clearly makes it evident that Cs_2AuInF_6 has a more stable structure than $Cs_2AuInCl_6$ for these compounds.

The total energy is minimized at E_0 = −82222.83 Ry and V = 1320.98 $Bohr^3$, as can be observed for Cs_2AuInF_6 in Fig. 2(a). Furthermore, as shown in Fig. 2(b), the lowest level of total energy for $Cs_2AuInCl_6$ is at E_0 = −86562.51 Ry and V = 2035.31 $Bohr^3$. The optimized bulk modulus (B_0) of the double perovskite material Cs_2AuInX_6 was shown to show how stiff it is, as shown in Table 1. This suggests that the structural rigidity of Cs_2AuInF_6 is greater than that of $Cs_2AuInCl_6$.

While the partial density of state (PDOS) shows how individual atoms or groups of atoms contribute to the vibrational modes, the total density of state (TDOS) represents the overall distribution of vibrational frequencies in the material. Fig. 3 displays the total and partial DOS of Cs_2AuInF_6 and $Cs_2AuInCl_6$. Positive and negative numbers are shown for both real and imaginary frequencies. In the composite Cs_2AuInX_6, the conduction band is mostly contributed by the halide atoms (X = F for Cs_2AuInF_6 and X = Cl for $Cs_2AuInCl_6$), although there is a smaller contribution from the In, Cs, and Au atoms in both materials. A strong peak is seen for flat bands in the PDOS of Cs_2AuInF_6 in the low-frequency region (below 1 kHz). However, the thermodynamic stability of Cs_2AuInF_6 is illustrated by the positive phonon frequencies throughout all Brillouin Zone (BZ) symmetry sites. On the other hand, the phonon dispersion of $Cs_2AuInCl_6$ reveals negative vibrational frequencies, indicating that the material is thermodynamically unstable. This means that the material's structure is not stable against small displacements of atoms, leading to a spontaneous distortion of the lattice. The material itself might be intrinsically unstable in the calculated phase. This could

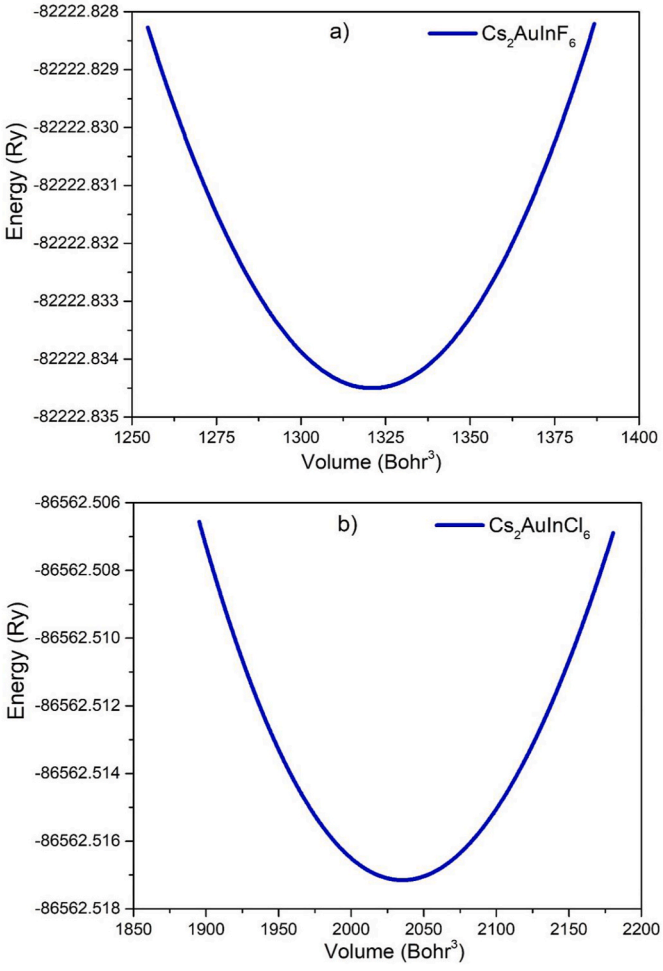

Fig. 2. Energy (E) versus unit cell volume (V) optimization curve of a) Cs_2AuInF_6 and b) $Cs_2AuInCl_6$.

be due to factors like strain, defects, or specific interatomic interactions that favor a different structure. At finite temperatures, thermal fluctuations can drive the system to explore different configurations, potentially leading to the stabilization of a new phase. Techniques like molecular dynamics simulations or the quasi-harmonic approximation can provide insights into temperature-induced stabilization. Although the structural stability of $Cs_2AuInCl_6$ is confirmed by formation energy.

3.2. *Mechanical stability and lattice thermal conductivity*

The assessment of the mechanical properties of the compound is dependent upon the important elastic constants C_{11}, C_{12} *and* C_{44} [39]. These constants allow the measurement of the compound's stability and its response to external pressures. To conduct an analysis on the mechanical characteristics of materials, it is essential to take into account the three elastic constants (C_{11}, C_{12} and C_{44}) as specified in Table 2. These constants are primarily applicable to cubic crystals.

The perovskite compound under consideration in the present work satisfies the Born Stability Criterion [40]: $C_{11} - C_{12} > 0$, $C_{11} - 2C_{12} > 0$, $C_{11} > B > C_{12}$, $C_{44} > 0$. When exposed to external pressures that result in deformation, as the materials Cs_2AuInF_6 and $Cs_2AuInCl_6$ under study do, these properties suggest that these materials possess elastic stability.

From an industrial perspective, many mechanical properties such as Bulk modulus (B), Shear modulus (G), Young's modulus (Y), Pugh's index (B/G), Poisson's ratio (σ), Cauchy's pressure (Cp) and Anisotropic ratio (A) have been computed and are displayed in Table 2. These parameters are additionally employed to examine the mechanical

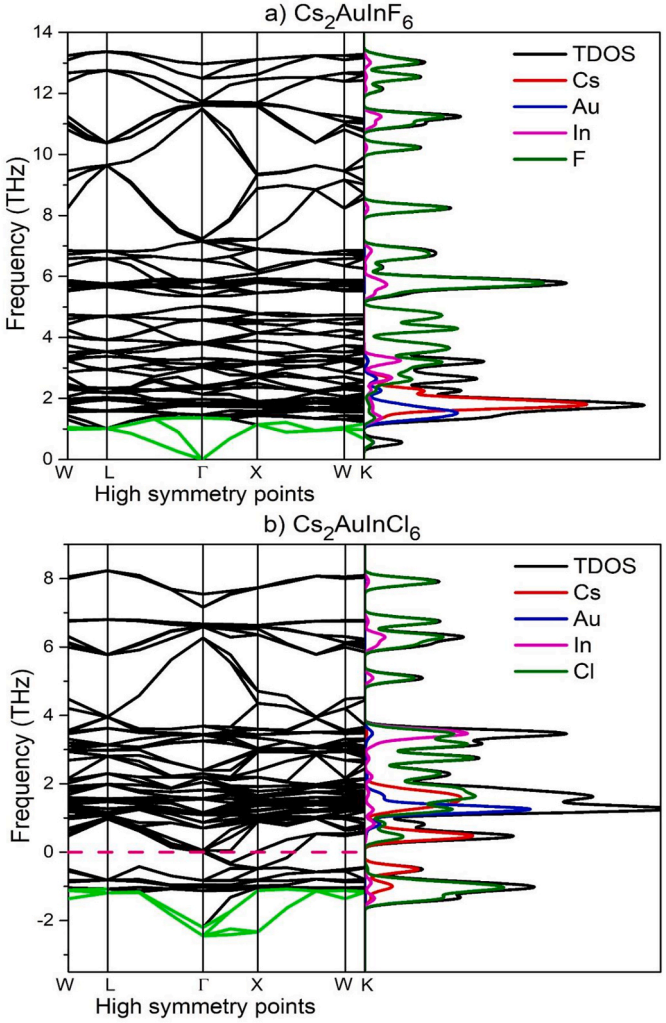

Fig. 3. Phonon dispersion with TDOS and PDOS of a) Cs_2AuInF_6 and b) $Cs_2AuInCl_6$ compound.

Table 2
Elastic parameter and mechanical stability of studied compounds.

Parameter	Cs_2AuInF_6	$Cs_2AuInCl_6$
C_{11} (GPa)	77.38	49.54
C_{12} (GPa)	37.78	21.92
C_{44} (GPa)	17.03	12.04
B (GPa)	50.98	31.13
G (GPa)	18.09	12.72
Y (GPa)	48.53	33.59
B/G	2.81	2.44
σ	0.34	0.32
$Cp = C_{12}–C_{44}$	20.75	9.88
$C' = (C_{11}–C_{12})/2$	19.80	13.81
A	0.86	0.87
Density, ρ (g/cm^3)	5.86	4.35
Elastic Debye temperature, Θ_D (K)	218.13	183.38
Transverse sound velocity, V_t (m/s)	1756	1710
Longitudinal sound velocity, V_l (m/s)	3578	3325
Averaged sound velocity, V_{av} (m/s)	1971	1914
Melting point, T_m (±300K)	1010.31	845.78
Minimum thermal conductivity, k_{min} (Wm^{-1}K^{-1})	0.37	0.27
Lattice thermal conductivity, k_L (Wm^{-1}K^{-1})	0.39	0.36

properties of the material.

The Shear modulus (G) and Bulk modulus (B) are obtained using the equations $G = \frac{G_V+G_R}{2}$ and $B = \frac{B_V+B_R}{2}$, respectively, where (B_R, G_R) and B_V, G_V) represent Reuss and Voigt bulk and shear moduli.

These are distinguished by the equations $G_V = \frac{C_{11}-C_{12}+3C_{44}}{5}$, $G_R = \frac{5C_{44}(C_{11}-C_{12})}{4C_{44}+3(C_{11}-C_{12})}$ and $B = B_V = B_R = \frac{C_{11}+2C_{12}}{3}$. The shear modulus (G) quantifies the extent of shear deformation exhibited by a material when subjected to external stress. The calculated G values for Cs_2AuInX_6 indicate a higher level of resistance to shear deformation.

Young's modulus (Y) can be mathematically expressed by the equation, $Y = \frac{9BG}{3B+G}$. As the value of Y increases, the material exhibits increasing stiffness. According to the data shown in Tables 2 and it can be observed that the current halide double perovskite exhibits a higher level of stiffness in comparison to $Cs_2ScInCl_6$ [7].

The B/G ratio and $Cp = C_{12} – C_{44}$ represent Pugh's ratio and Cauchy's pressure, respectively, which establish the ductile and brittle characteristics shown by the material Cs_2AuInX_6. According to Pugh's ratio, materials with values beyond 1.75 are classified as ductile, while those with values below 1.75 are considered brittle [41]. The values of Pugh's ratio for both Cs_2AuInF_6 and $Cs_2AuInCl_6$ in Table 2 exceeds 1.75 for the current compound, indicating the presence of ductile characteristics in the material.

According to Ref. [42], the material exhibits ductile behavior when the value of Cp is positive, but it demonstrates brittle behavior when the value is negative. As per the data presented in Tables 2 and it can be observed that the value of Cp is greater than zero, indicating that the material exhibits ductile characteristics. The ductile behavior is further substantiated by the Poisson ratio $\boldsymbol{\sigma}$, which can be determined using the formula $\sigma = \frac{3B-Y}{6B}$ [43]. When $\boldsymbol{\sigma}$ surpasses the value of 0.26, the material exhibits ductile behavior. Table 2 reveals that the values of $\boldsymbol{\sigma}$ for both Cs_2AuInF_6 and $Cs_2AuInCl_6$ exceed 0.26, hence implying a ductile characteristic. The Poisson ratio ($\boldsymbol{\sigma}$) is a parameter that quantifies the crystal's ability to withstand shear stress, a property that is connected to its elasticity. Materials that possess smaller $\boldsymbol{\sigma}$ values have a greater level of stability when exposed to shear stress.

The elastic constants are used to determine the melting point and Debye temperatures, whereas the equation provided in Ref. [44] can be employed to calculate the melting temperature, $T_m = (553 + 5.911C_{11}) \pm 300K$ and the Debye temperature, $\Theta_D = \frac{h}{k_B}\left[\frac{3nN_A\rho}{4\pi M}\right]^{1/3} V_m$. Energy conversion efficiency can be affected by higher Debye temperatures, which increase atomic bonding and thermal stability.

The ultrasonic wave velocities of the double perovskite are determined using the utilization of solid-state electrochemical cells. The magnitudes of longitudinal (V_l) and transversal (V_t) modes of sound velocities are calculated using the formulas $V_l = \sqrt{\frac{3B+4G}{3\rho}}$ and $V_t = \sqrt{\frac{G}{\rho}}$, respectively. Thus, average sound velocity (V_{av}) is computed using these velocities in equation $V_{av} = \left[\frac{1}{3}\left(\frac{2}{V_t^3}+\frac{1}{V_l^3}\right)\right]^{-1/3}$. Moreover, the Cahill formula has been used to calculate the minimum value of thermal conductivity (k_{min}) [45]:

$$k_{min} = \frac{K}{2.48} n_b^{\frac{2}{3}} (V_l - 2V_t)$$

A low value of thermal conductivity reduces the internal heat generation of the devices, which typically would cause material damage and lower efficiency [46]. Double perovskite materials with thermal conductivity can increase power conversion efficiency in solar cell applications, by reducing heat dissipation [47]. Also, waste heat can be turned back into useful energy by efficiently moving heat from a source to a heat sink using such materials with low thermal conductivity. The lattice part of thermal conductivity is calculated with the help of Slack's equation [48]:

$$k_L = \frac{A\Theta_D^3 V^{1/3} m}{\Upsilon^2 \overline{N}^{2/3} T}$$

Temperature (T), volume (V), average molar mass per atom (m), Grüneisen parameter (ϒ), number of atoms per unit cell ($\overline{N}$), Debye temperature (Θ_D), and temperature (T) are all said to be dependent on K_L in the formula. The relationship between lattice thermal conductivity and temperature of the studied materials Cs_2AuInF_6 and $Cs_2AuInCl_6$ is graphed across a range of 200–1000K and presented in Fig. 4.

3.3. Electronic properties and the effective mass of charge carrier with DOS

This section provides an elucidation of the calculations associated with the band structures and density of states of the compound Cs_2AuInX_6 (X = F,Cl). Fig. 5 displays the band structures, revealing a direct band gap semiconductor characteristic due to the alignment of the conduction band (CB) minimum and valence band (VB) maximum at the symmetrical point Γ for each compound, which are 0.51 eV for Cs_2AuInF_6 and 0.29 eV for $Cs_2AuInCl_6$, as determined by TB-mBJ. Additionally, when the compounds are calculated using GGA-PBE, the results are zero (0 eV) for both of them, and it is found that the states overlap from the valence band to the conduction band and vice versa. In this study, the TB-mBJ approximation has been taken into consideration as it provides a better band gap value in comparison to the GGA-PBE approximation. The GGA-PBE approximation tends to underestimate the band gap in systems containing d-orbitals. In contrast, the TB-mBJ approximation has been found to produce results that closely align with experimental values, as described in the literature [49–51]. In addition, we reproduced the band gap of such types of materials using the GGA-PBE and TB-mBJ approximation methods to ensure the accuracy of our calculations, as shown in Table 3.

When a semiconductor material has a direct band gap, the Brillouin zone occurs at the same momentum where the least amount of energy needed for an electron to move from the valence band to the conduction band occurs [20]. There is not much energy lost in the formation of these electron-hole pairs, resulting in a high power conversion efficiency. This efficient light absorption is necessary for photovoltaic energy-collecting solar cells to function.

Besides, the band gap diminishes from 0.51 eV to 0.29 eV from F to Cl due to the increasing ionic radius of the halide ions at the center of octahedrons. The larger size of the halide ions results in a smaller difference between the valence and conduction bands. Furthermore, according to band structure, states are comparatively unvarying and

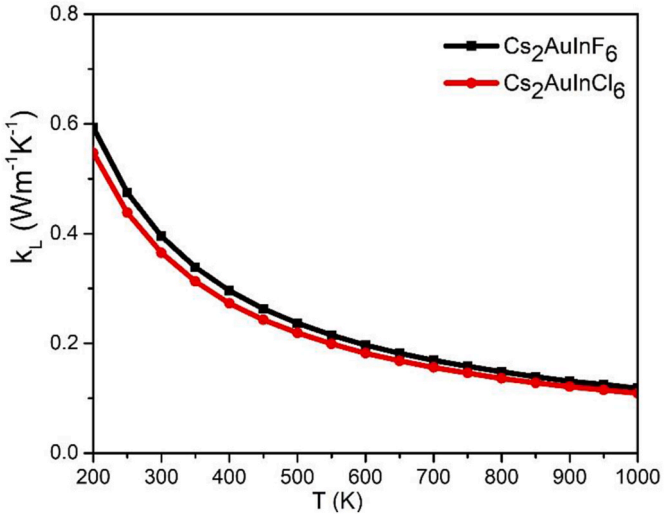

Fig. 4. Lattice thermal conductivity (k_L) of Cs_2AuInF_6 and $Cs_2AuInCl_6$.

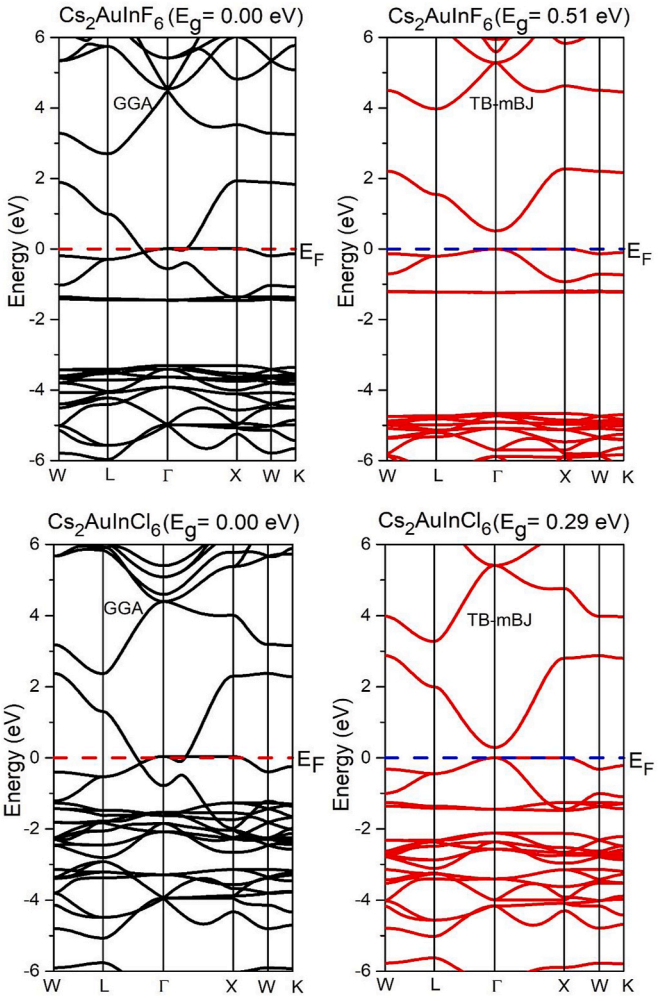

Fig. 5. Band structure of Cs_2AuInF_6 and $Cs_2AuInCl_6$ computed by GGA-PBE (Left side) and TB-mBJ (Right side) approach.

Table 3
Computed band gaps for Cs_2AuInF_6 and $Cs_2AuInCl_6$.

Compound	GGA-PBE	TB-mBJ	Nature	References
Cs_2AuInF_6	0	0.51	direct	This work
$Cs_2AuInCl_6$	0	0.29	direct	This work
$Cs_2ScInCl_6$	0.518	0.632	direct	This work
	0.532	0.637	direct	[7]
$Cs_2ScInBr_6$	0.712	0.805	direct	This work
	0.73	0.81	direct	[52]

numerous in the valence band but curved and few in number in the conduction band, as per TB-mBJ. It suggests that these materials are p-type since their effective mass m_h is larger than their electron mass m_e, as listed in Table 4. Since Cs_2AuInX_6 (X = F/Cl) exhibits a direct band gap, allowing efficient radiative recombination where electrons from the conduction band recombine with holes in the valence band, emitting photons. This radiative recombination is responsible for luminescence in

Table 4
Estimated effective masses of holes (m_h*) and electrons (m_e*) of Cs_2AuInF_6 and $Cs_2AuInCl_6$.

Compound	Approach	m_h^*/m_0	m_e^*/m_0
Cs_2AuInF_6	TB-mBJ	1.19	0.17
$Cs_2AuInCl_6$	TB-mBJ	0.36	0.083

light-emitting (optical) applications. The efficiency of this process depends on the quality of the crystal and the absence of non-radiative pathways.

In double perovskite materials, the effective mass of charge carriers describes the inertia of charge carriers, such as electrons or holes, inside the material's crystal lattice. Smaller effective mass charge carriers move more readily in response to an applied electric field, increasing charge transport and energy conversion efficiency. Using the E-K dispersion of the material Cs_2AuInX_6, the effective mass and hole are computed using the following formula:

$$m^* = \frac{\hbar^2}{(d^2E/dK^2)}$$

Where, $\hbar = 1.05 \times 10^{-34}$ J/s in this case. We obtain the values of d^2E/dK^2 from the E-K dispersion curve by fitting the corresponding parabolic curve at any symmetry points with it. A reduction in effective mass can potentially lead to an increase in carrier mobility. The study of the effective mass of electrons and the charge carriers (both electrons and halides) characteristics of double perovskite materials is of considerable significance in the understanding of their electronic properties. The material allows electrons to move quickly and freely because of its low effective masses of electrons (0.17/0.083 for Cs_2AuInF_6/$Cs_2AuInCl_6$, respectively) as listed in Table 4. Double perovskites are excellent choices for solar cell applications because of their high electron mobility and efficient charge transfer because of their low effective mass of electron.

Moreover, Fig. 6 depicts the distribution of electrons in Cs_2AuInF_6 and $Cs_2AuInCl_6$ by plotting the total and partial density of states (DOS). Both the band structure and the total DOS exhibit the same pattern. In general, DOS plots illustrate the several energy levels that contribute to the creation of a band, and more precisely, the material's transport properties. The Cs-*p* and F-*p* states contribute the most to the lower valence band of the complex Cs_2AuInF_6, whereas the Cs-*d*, Au-*d*, and In-*d* states have less contributions. In the upper valence band, Cs_2AuInF_6 has substantial contributions from Au-*d* and F-*p* states, whereas $Cs_2AuInCl_6$ shows notable contributions from Au-*d* and Cl-*p* states. However, Cs_2AuInF_6 is mostly influenced by In-*s* and F-*p* states in the lower conduction band, whereas In-*s* and Cl-*p* states have significant contributions for $Cs_2AuInCl_6$.

3.4. Optical properties

A material's light-to-electric energy conversion efficiency, band gap, and energy absorption capacity define its photovoltaic and solar cell properties. Because they increase the usefulness of optical systems by eliminating phonon emission by direct electron translation between the valence band and conduction band, direct band gaps are especially significant. The dielectric constant, $\varepsilon(\omega)$, is used to study the relationship between light and matter. The real part $\varepsilon_1(\omega)$ and imaginary part $\varepsilon_2(\omega)$ of the dielectric constant, which are obtained using Kramer-Kronig relations and provided by equations in Refs. [53–55], are used to describe the additional optical properties.

Fig. 7(a) shows the static value of the real part of the dielectric function, $\varepsilon_1(\omega)$, which represents the static characteristics of the compound Cs_2AuInX_6. Because $Cs_2AuInCl_6$ has a lower band gap than Cs_2AuInF_6, it consequently possesses a greater static dielectric function. As photon energy increases, $\varepsilon_1(\omega)$ increases as well, peaking in the visible spectrum range. It reaches to its minimum in the UV spectrum after which there is again an increasing trend. Fig. 7(b) shows the imaginary part of the dielectric function, $\varepsilon_2(\omega)$. When the anion is switched from Cl to F, a larger value towards the lower energy level is created. The highest peak of Cs_2AuInF_6 is observed in the energy level from 1 eV to 2.5 eV.

The refractive index, n(ω), is shown in Fig. 7(c). Because of their interaction, the refractive index spectra show a pattern of $\varepsilon_1(\omega)$, with

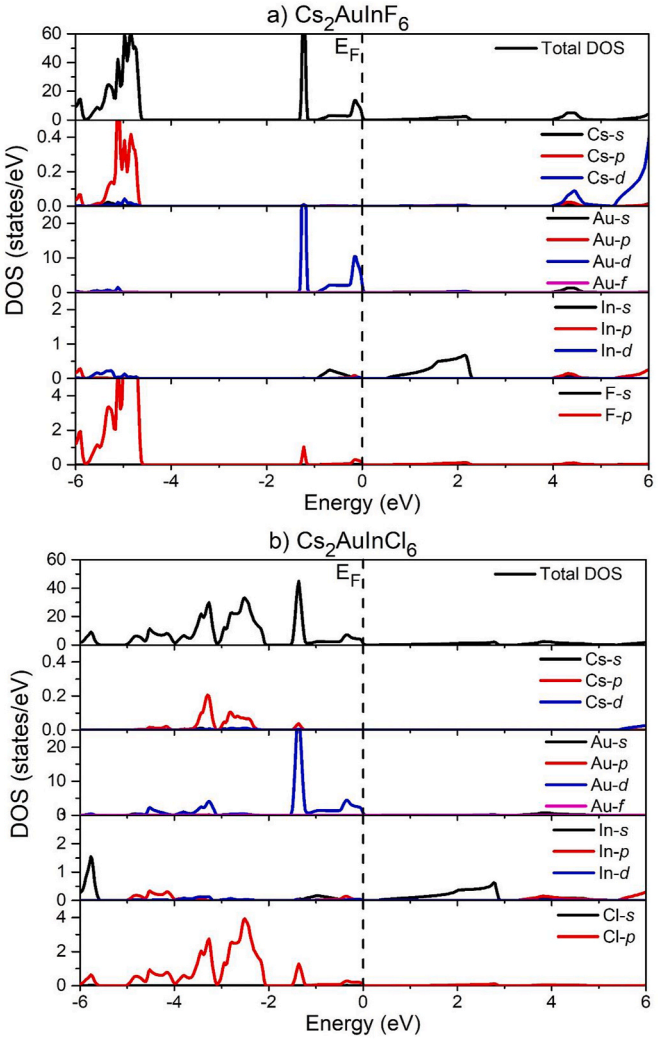

Fig. 6. Density of states: Total and partial of a) Cs_2AuInF_6 and b) $Cs_2AuInCl_6$.

different magnitudes. Between Cs_2AuInF_6 and $Cs_2AuInCl_6$, the refractive index of $Cs_2AuInCl_6$ is slightly higher in the low-frequency region. The upper visible light spectrum is where the refractive index is largest, and as one moves towards the ultraviolet region, it rapidly decreases. It is apparent that the small band gap of $Cs_2AuInCl_6$ accounts for its marginally higher static refractive index spectra than those of Cs_2AuInF_6, which are 1.95 and 1.90, respectively, and are comparable to the silicon nitride (1.90) solar cells [56]. Table 5 displays the calculated values for the real components of the dielectric constant $\varepsilon_1(0)$, refractive index n(0), optical reflectivity R(0) and maximum absorption coefficient.

The amount of absorption per optical medium unit length shown in Fig. 7(d) is given by the absorption coefficient of that material, which shows how much light at a given wavelength will reach the material before absorption, which is used to calculate the solar energy conversion efficiency. The equation of absorption co-efficient, I(ω) is as below [57] -

$$I(\omega) = \sqrt{2}\left[\sqrt{\varepsilon_1(\omega)^2 + \varepsilon_2(\omega)^2} - \varepsilon_1(\omega)\right]^{1/2}$$

When compared to the material $Cs_2AuInCl_6$, the compound Cs_2AuInF_6 exhibits the first highest peak between 1.75eV and 3.11eV which is known as the optical visible light range. In the energy range of 1 eV–3 eV for Cs_2AuInF_6 and 2 eV–3.5 eV for $Cs_2AuInCl_6$, the photons are significantly absorbed. The material Cs_2AuInX_6 (X = F/Cl) exhibits absorption coefficients of 2.24×10^5 cm^{-1} at 2.95 eV for $Cs_2AuInCl_6$ and

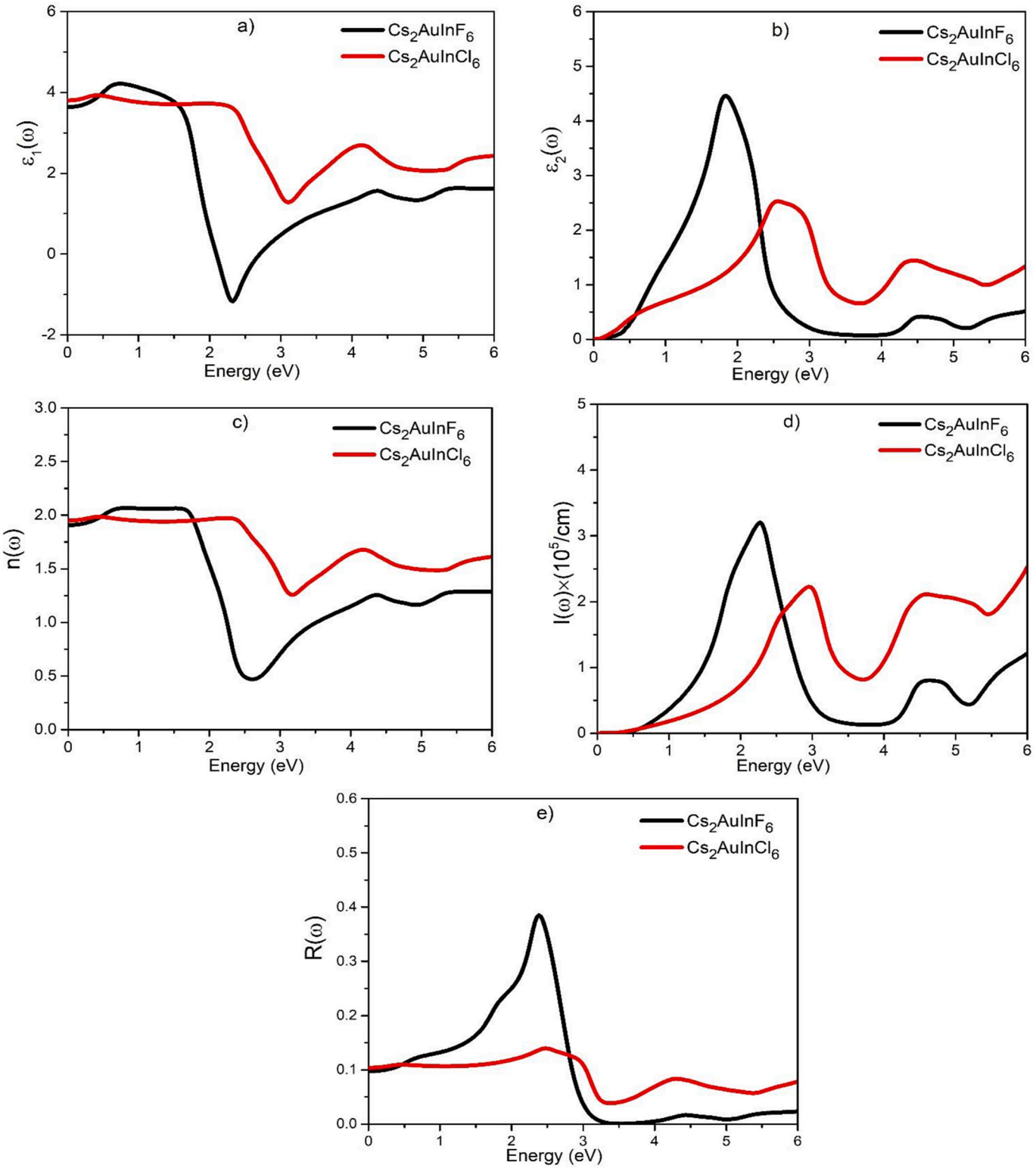

Fig. 7. a) Real part of the dielectric function: $\boldsymbol{\varepsilon_1(\omega)}$ b) Imaginary part of the dielectric function: $\boldsymbol{\varepsilon_2(\omega)}$ c) Refractive index: ***n(ω)*** d) Absorption coefficient: ***I(ω)*** and e) Optical reflectivity: ***R(ω)*** of studied compound.

Table 5
Computed optical constants.

Compound	$\boldsymbol{\varepsilon_1(0)}$	*n(0)*	*R(0)*	$I_{max}(\omega)\times10^5$
Cs_2AuInF_6	3.64	1.90	0.09	3.21
$Cs_2AuInCl_6$	3.80	1.95	0.10	2.24

3.21×10^5 cm^{-1} at 2.27 eV for Cs_2AuInF_6, respectively. These values indicate that the materials are capable of serving as potent absorbers in the visible spectrum (400–700 nm). In addition, our studied materials exhibit higher absorption coefficients compared to other DPs (10^4 order), such as Cs_2CuBiX_6 (X = Cl/Br/I) [58], Cs_2AgBiI_6 [59] and Cs_2InCoX_6 [60]. The materials under investigation are also consistent

with commercially available absorbent materials, including Si (10^3 to 10^5 cm^{-1}), CdTe (10^4 to 10^5 cm^{-1}), and CIGS (10^4 to 10^5 cm^{-1}) [61].

The dielectric characteristics of the compounds are used to compute other essential optical constants, such as the refractive factor n(ω), the extinction factor k(ω), and the reflectivity R(ω) [62–64].

$$n(\omega)=\left[\frac{\{\varepsilon_1^2(\omega)+\varepsilon_2^2(\omega)\}^{\frac{1}{2}}}{2}+\frac{\varepsilon_1(\omega)}{2}\right]^{1/2}$$

$$k(\omega)=\left[\frac{\{\varepsilon_1^2(\omega)+\varepsilon_2^2(\omega)\}^{\frac{1}{2}}}{2}-\frac{\varepsilon_1(\omega)}{2}\right]^{1/2}$$

$$R(\omega)=\frac{\{n(\omega)-1\}^2+k^2(\omega)}{\{n(\omega)+1\}^2+k^2(\omega)}$$

Fig. 7(e) displays the optical reflectivity of the current compound of this study. Due to the comparatively lower energy bandgap of $Cs_2AuInCl_6$ in comparison to Cs_2AuInF_6, it has slightly high reflectivity at the beginning. However, the Cs_2AuInF_6 has the first highest peak in the optical visible light region.

Direct bandgap compounds enable minimum photon interaction in the direct optical transition between the valence band and conduction band. In the area of bandgap energy, this leads to a sharp absorption edge and high absorption coefficient. likewise, only lower energy photons can be absorbed by materials having a small bandgap, whereas higher energy photons can be absorbed by materials with a large bandgap. The reflectance of materials is affected by this variation. With a bandgap that is comparably larger than that of Cs_2AuInF_6, the double perovskite compound Cs_2AuInF_6 exhibits increased reflectivity in the visible light-corresponding low energy portion of the spectrum, which is between 0 and 3 eV. This is due to the fact that photons with energy below the bandgap are reflected instead being absorbed. Reflectivity lowers as photon energy rises, increasing the amount of photons with energies over the bandgap that may be absorbed.

3.5. Thermoelectric properties

This section focuses on converting thermoelectric energy efficiently in materials by adjusting their temperature. In order to assess the suitability of a material for utilization in devices, it is necessary to study several transport parameters, including electrical conductivity (σ), electronic thermal conductivity (k_e), Seebeck coefficient (S), power factor (PF), and the figure of merit (ZT), using the aid of the BoldTrap2 code [31]. For the temperature range of 200–1000K, all of these transport parameters are calculated in Table 6 and displayed in Fig. 8(a–d).

The electrical conductivity in relation to temperature is displayed in Fig. 8(a). It shows a linear increase in the electrical conductivity from $0.43/0.40 \times 10^{19}$ (200 K) to $1.57/1.81 \times 10^{19}$ [1/(Ω*m*s)] (1000 K) for $Cs_2AuInF_6/Cs_2AuInCl_6$ respectively. At room temperature (300 K), the electrical conductivity is $0.66/0.62 \times 10^{19}$ [1/(Ω*m*s)] for $Cs_2AuInF_6/Cs_2AuInCl_6$, respectively, while the intersection point is 1.12×10^{19} [1/(Ω*m*s)] (550 K).

Thermal conductivity is the next key property that measures heat transport through a substance. The total lattice thermal conductivity has two distinct constituents: the lattice component, resulting from lattice vibrations, and the electronic component, arising from charge carriers which can be written as [65]:

$$k=k_e+k_L$$

Here, k_L stands for lattice thermal conductivity which has not calculate in this section due to the incapacity of BoldTrap2 and separately shown in the 3.2 section by using Glen A. Slack equation. Fig. 8(b) illustrates the relationship between electronic thermal conductivity and temperature for current perovskite compounds, indicating that k_e increases as temperature rises. The temperature-dependent behavior of the compound Cs_2AuInX_6 (X = F/Cl) indicates its semiconducting nature. Furthermore, Fig. 8(b) shows that the compound $Cs_2AuInCl_6$ has a steeper curve compared to that of Cs_2AuInF_6. Table 6 presents the transport parameter values of the double perovskites being examined at a temperature of 300 K.

Another important measure is the Seebeck coefficient (S), whose positive number indicating holes as predominant carriers qualifies a compound as a p-type semiconductor. The predicted Seebeck coefficient (S) against temperature is displayed in Fig. 8(c). Furthermore, initially Cs_2AuInF_6 has a larger Seebeck coefficient value than that of $Cs_2AuInCl_6$. The values of the two materials significantly drop after reaching room temperature (300 K), with the interaction point value being 0.21 (mV/K) at 250 K. Furthermore, the thermoelectric performance of the studied perovskite materials is dependent on two parameters, electrical conductivity (σ) and seebeck coefficient (S), which are measured by the power factor (PF). Enhancing the thermoelectric performance of double perovskites requires a large amount of S. Without accounting for the influence of K, the power factor (PF) has been estimated as (σS^2) in order to understand the thermoelectric performance of this study. Fig. 8(d) displays that the PF increases from $2.03/1.84 \times 10^{11}$ ($Wm^{-1}K^{-2}s^{-1}$) when T increases from 200 to 1000 K while the intersection point is 3.08×10^{11} ($Wm^{-1}K^{-2}s^{-1}$) (350 K) for $Cs_2AuInF_6/Cs_2AuInCl_6$, respectively.

One specific characteristic that can be used to empirically describe a thermoelectric material's performance is its figure of merit (ZT). However, the identification of thermoelectric performance is incomplete unless the contribution of lattice thermal conductivity (k_L) is taken into account, which is the most important part in calculating the value of ZT and is given by the following equation by its dimensionless form [66].

$$ZT=\frac{\sigma S^2}{k_e+k_L}$$

The efficiency of a thermoelectric material can be raised by increasing its ZT value. In order to be the optimal selection, ZT needs to be one or higher. Additionally, a higher value of ZT can be attained by reducing the value of total thermal conductivity (k). The plot of the Figure of merit is shown in Fig. 9. At room temperature (300 K), the ZT are observed at 0.43 and 0.42, and maximum values are 0.47 and 0.46 for Cs_2AuInF_6 and $Cs_2AuInCl_6$ at 400 K, respectively. The graphs of Fig. 9 for both materials are nearly identical, with ZT increasing up to 450 K and decreasing as temperature rises.

Table 6
Electrical conductivity: **(σ/τ)**, electronic conductivity: **(k_e/τ)**, See-beck coefficient: **S**, power factor: **PF**, Figure of merit: **ZT** of the investigated compounds at 300K.

Compound	(σ/τ) × 10^{19} (1/Ω.m.s)	(k_e/τ) × 10^{14} ($Wm^{-1}K^{-1}s^{-1}$)	S (mV/K)	PF (× 10^{11}) ($Wm^{-1}K^{-2}s^{-1}$	ZT
Cs_2AuInF_6	0.66	0.26	0.205	2.80	0.43
$Cs_2AuInCl_6$	0.62	0.28	0.208	2.68	0.42

4. Conclusion

For the double perovskite material Cs_2AuInX_6 (X = F/Cl), DFT is used, by which the ground state energy has been found with the aid of the Wien2K code. It is seen that the values of the lattice constants increase by replacing the anions from F to Cl. The calculated higher values of bulk modulus, shear modulus, and Young's modulus for the studied compound confirm its stiffness and rigidity. The Debye temperature and melting points are 218.13K/183.38K and 1010.3K/845.7K for Cs_2AuInF_6 and $Cs_2AuInCl_6$, respectively. However, the material $Cs_2AuInCl_6$ is found mechanically stable but thermodynamically

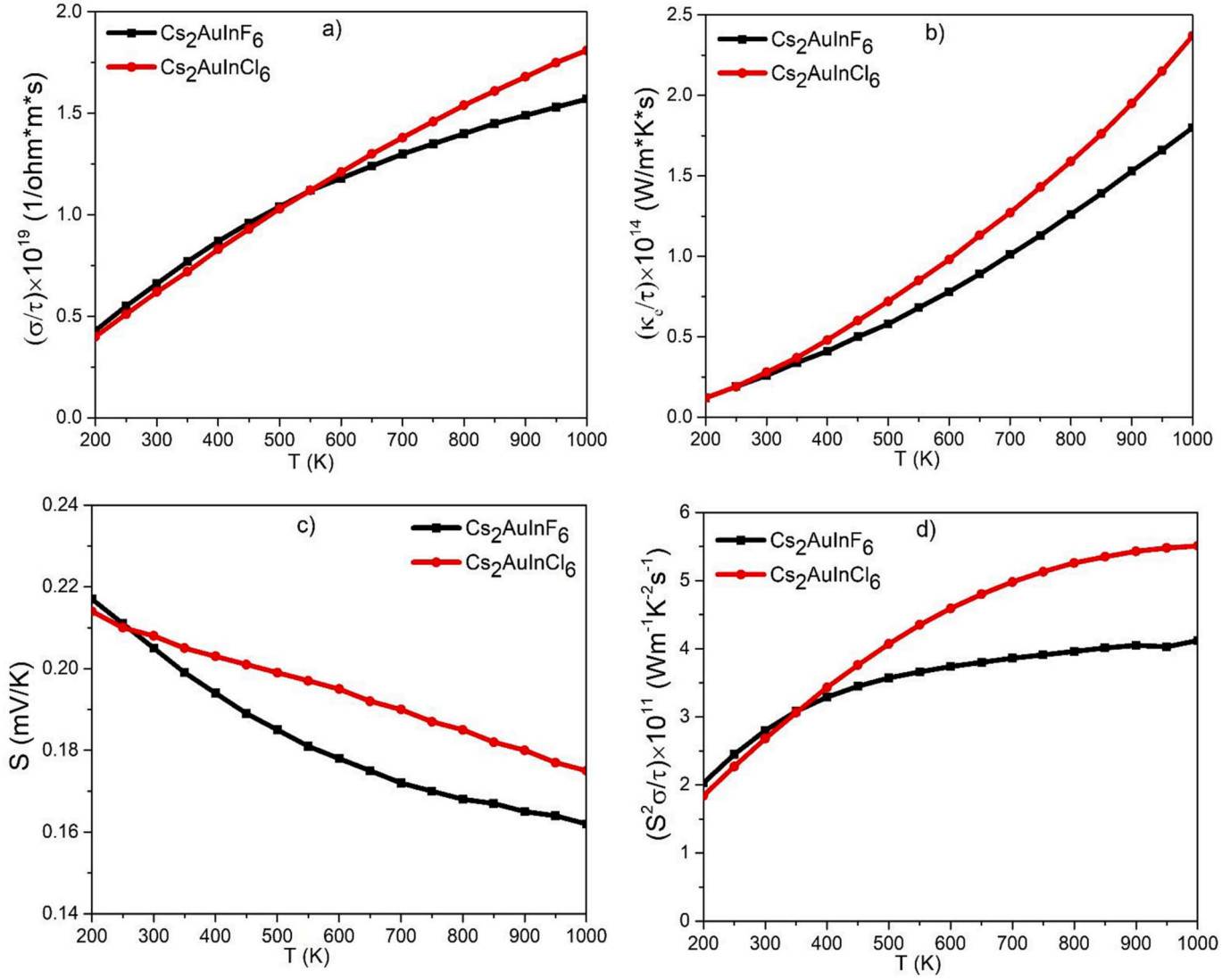

Fig. 8. The calculated a) Electrical conductivity, σ/τ, b) Electronic thermal conductivity, k_e/τ, c) See-beck coefficient, S, and d) Power factor, $S^2\sigma/\tau$, of the studied compounds.

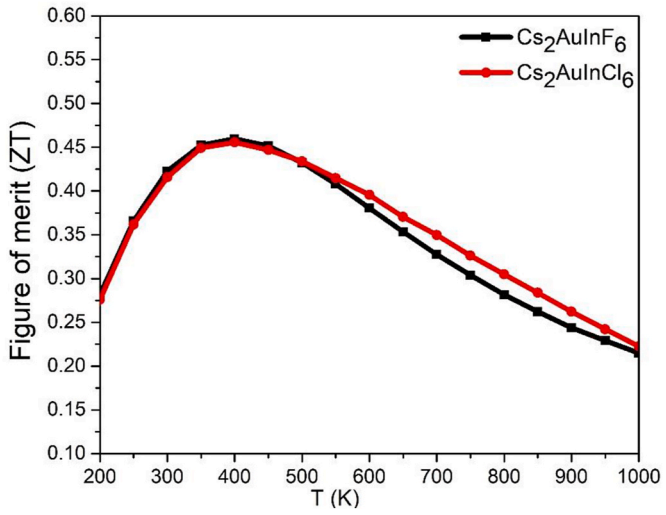

Fig. 9. Figure of merit (ZT) of the studied compounds.

unstable by phonon dispersion; because of this, further research is needed in this regard. The ductility of the studied compounds is validated by their elastic properties, which is crucial for the manufacture of devices. Using the TB-mBJ approximation to look at the energy band structure, it shows that the materials are direct and have small band gap. They are good at absorbing both infrared to visible light, which makes them good choices for solar cell applications and IR photodetectors. In addition, their low effective mass of electrons (0.17/0.083 for Cs_2AuInF_6 and $Cs_2AuInCl_6$, respectively) makes them a good choice for solar photovoltaic applications due to their strong electron mobility and effective charge transfer. The compound Cs_2AuInF_6 responds to the incident photon with considerable absorption in the optical visible light range of 1.75 eV–3.11 eV, as demonstrated by its important optical constants when the compound $Cs_2AuInCl_6$ is compared to it. The absorption coefficients of the titled materials, respectively, are 3.21×10^5 cm^{-1} at 2.27 eV and 2.24×10^5 cm^{-1} at 2.95 eV. Notably, the maximum values of the actual figures of merit of the compounds under investigation, Cs_2AuInX_6 (X = F/Cl), are 0.47 and 0.46 at a temperature of 400 K, respectively. Finally, the outcomes of the studied DP halide analysis are promising and should offer appropriate direction for further study on IR photodetector and solar energy applications.

CRediT authorship contribution statement

S. Mahmud: Writing – original draft, Validation, Methodology, Formal analysis, Data curation, Conceptualization. **M.A.U.Z. Atik:** Writing – original draft, Validation, Resources, Methodology, Formal analysis. **M.N. Mostakim:** Writing – review & editing, Validation, Resources, Investigation. **Md. Tarekuzzaman:** Writing – review & editing, Validation. **Md. Zahid Hasan:** Writing – review & editing, Validation, Formal analysis.

Declaration of competing interest

The authors declare that they have no known competing financial interests or personal relationships that could have appeared to influence the work reported in this paper.

Data availability

Data will be made available on request.

References

[1] O.B. Awodumi, A.O. Adewuyi, The role of non-renewable energy consumption in economic growth and carbon emission: evidence from oil producing economies in Africa, Energy Strategy Rev. 27 (2020) 100434.

[2] M.M. Asghar, Z. Wang, B. Wang, S.A.H. Zaidi, Nonrenewable energy—environmental and health effects on human capital: empirical evidence from Pakistan, Environ. Sci. Pollut. Res. 27 (2020) 2630–2646.

[3] M. Dada, P. Popoola, Recent advances in solar photovoltaic materials and systems for energy storage applications: a review, Beni-Suef Univ. J. Basic Appl. Sci. 12 (1) (2023) 1–15.

[4] I. Kougias, et al., Analysis of emerging technologies in the hydropower sector, Renew. Sustain. Energy Rev. 113 (2019) 109257.

[5] A. Kumar, M.Z.U. Khan, B. Pandey, S. Mekhilef, Wind energy: a review paper, Gyancity J. Eng. Technol. 4 (2) (2018) 29–37.

[6] J.S. Manser, J.A. Christians, P. V Kamat, Intriguing optoelectronic properties of metal halide perovskites, Chem. Rev. 116 (21) (2016) 12956–13008.

[7] S.A. Dar, B. Want, Direct band gap double perovskite halide $Cs_2ScInCl_6$ for optoelectronic applications—a first principle study, Comput. Condens. Matter 33 (August) (2022) e00736, https://doi.org/10.1016/j.cocom.2022.e00736.

[8] H. Wang, W. Su, J. Liu, C. Wang, Recent development of n-type perovskite thermoelectrics, J. Mater. 2 (3) (2016) 225–236.

[9] M. Saxena, K. Tanwar, T. Maiti, Environmental friendly Sr_2TiMoO_6 double perovskite for high temperature thermoelectric applications, Scripta Mater. 130 (2017) 205–209.

[10] T. Tang, Y. Tang, First principle comparative study of transitional elements Co, Rh, Ir (III)-based double halide perovskites, Mater. Today Commun. 34 (2023) 105431.

[11] T. Tang, Y. Tang, Electronic structure, mechanical properties and optical properties of three cobalt-based double halide perovskites: a first-principles study, J. Phys. Chem. Solid. 179 (2023) 111415.

[12] A. Harbi, M. Moutaabbid, Thermoelectric and optoelectronic properties of novel lead-free halide perovskites Cs_2RbTiX_6 (X= I, Br and Cl) for photovoltaic applications, Comput. Condens. Matter 32 (2022) e00733.

[13] M.U. Din, J. Munir, M. Jamil, M.A. Saeed, Q. Ain, Electronic structure and optical response of double perovskite Rb_2NaCoF_6 for optoelectronic devices, Phys. B Condens. Matter 627 (2022) 413533.

[14] A. Menedjhi, N. Bouarissa, S. Saib, K. Bouamama, Halide double perovskite $Cs_2AgInBr_6$ for photovoltaic's applications: optical properties and stability, Optik 243 (2021) 167198.

[15] Y. Liu, A. Nag, L. Manna, Z. Xia, Lead-free double perovskite $Cs_2AgInCl_6$, Angew. Chem. 133 (21) (2021) 11696–11707.

[16] K. Wang, Y. He, M. Zhang, J. Shi, W. Cai, Promising lead-free double-perovskite photovoltaic materials $Cs_2MM'Br_6$ (M= Cu, Ag, and Au; M′= Ga, in, Sb, and Bi) with an ideal band gap and high power conversion efficiency, J. Phys. Chem. C 125 (38) (2021) 21160–21168.

[17] N.R. Wolf, B.A. Connor, A.H. Slavney, H.I. Karunadasa, Doubling the stakes: the promise of halide double perovskites, Angew. Chem. 133 (30) (2021) 16400–16414.

[18] L.A. Muscarella, E.M. Hutter, Halide double-perovskite semiconductors beyond photovoltaics, ACS Energy Lett. 7 (6) (2022) 2128–2135.

[19] S. Mahmud, M.A. Ali, M.M. Hossain, M.M. Uddin, DFT aided prediction of phase stability, optoelectronic and thermoelectric properties of A_2AuScX_6 (A= Cs, Rb; X= Cl, Br, I) double perovskites for energy harvesting technology, Vacuum (2023) 112926.

[20] G. Murtaza, et al., Lead free double perovsites halides $X_2AgTlCl_6$ (X= Rb, Cs) for solar cells and renewable energy applications, J. Solid State Chem. 297 (2021) 121988.

[21] N.A. Noor, et al., Analysis of direct band gap A_2ScInI_6 (A= Rb, Cs) double perovskite halides using DFT approach for renewable energy devices, J. Mater. Res. Technol. 13 (2021) 2491–2500.

[22] F. Aslam, H. Ullah, M. Hassan, Theoretical investigation of Cs_2InBiX_6 (X= Cl, Br, I) double perovskite halides using first-principle calculations, Mater. Sci. Eng. B 274 (2021) 115456.

[23] Y. Saeed, et al., $Cs_2NaGaBr_6$: a new lead-free and direct band gap halide double perovskite, RSC Adv. 10 (30) (2020) 17444–17451.

[24] A. Bala, V. Kumar, Direct band gap halide-double-perovskite absorbers for solar cells and light emitting diodes: ab initio study of bulk and layers, Phys. Rev. Mater. 5 (9) (2021) 95401.

[25] S. Iqbal, et al., Tuning the optoelectronic and thermoelectric characteristics of narrow bandgap Rb_2AlInX_6(X= Cl, Br, I) double perovskites: a DFT study, Mater. Sci. Semicond. Process. 143 (2022) 106551, https://doi.org/10.1016/j.mssp.2022.106551.

[26] N.P. Mathew, N.R. Kumar, R. Radhakrishnan, First principle study of the structural and optoelectronic properties of direct bandgap double perovskite $Cs_2AgInCl_6$, Mater. Today Proc. 33 (2020) 1252–1256.

[27] K. Schwarz, DFT calculations of solids with LAPW and WIEN2k, J. Solid State Chem. 176 (2) (2003) 319–328.

[28] J.P. Perdew, K. Burke, M. Ernzerhof, Generalized gradient approximation made simple, Phys. Rev. Lett. 77 (18) (1996) 3865.

[29] M. Jamal, M. Bilal, I. Ahmad, S. Jalali-Asadabadi, IRelast package, J. Alloys Compd. 735 (2018) 569–579.

[30] K. Nakano, T. Sakai, Assessing the performance of the Tran–Blaha modified Becke–Johnson exchange potential for optical constants of semiconductors in the ultraviolet–visible light region, J. Appl. Phys. 123 (1) (2018).

[31] G.K.H. Madsen, J. Carrete, M.J. Verstraete, BoltzTraP2, a program for interpolating band structures and calculating semi-classical transport coefficients, Comput. Phys. Commun. 231 (2018) 140–145, https://doi.org/10.1016/j.cpc.2018.05.010.

[32] F. Birch, Finite elastic strain of cubic crystals, Phys. Rev. 71 (11) (1947) 809.

[33] C. Li, X. Lu, W. Ding, L. Feng, Y. Gao, Z. Guo, "Formability of abx_3 (x= f, cl, br, i) halide perovskites,", Acta Crystallogr. Sect. B Struct. Sci. 64 (6) (2008) 702–707.

[34] A.E. Fedorovskiy, N.A. Drigo, M.K. Nazeeruddin, The role of Goldschmidt's tolerance factor in the formation of A_2BX_6 double halide perovskites and its optimal range, Small Methods 4 (5) (2020) 1900426.

[35] R.D. Shannon, Revised effective ionic radii and systematic studies of interatomic distances in halides and chalcogenides, Acta Crystallogr. Sect. A Cryst. physics, diffraction, Theor. Gen. Crystallogr. 32 (5) (1976) 751–767.

[36] S. Zhao, K. Yamamoto, S. Iikubo, S. Hayase, T. Ma, First-principles study of electronic and optical properties of lead-free double perovskites Cs_2NaBX_6 (B= Sb, Bi; X= Cl, Br, I), J. Phys. Chem. Solid. 117 (2018) 117–121.

[37] X. Du, D. He, H. Mei, Y. Zhong, N. Cheng, Insights on electronic structures, elastic features and optical properties of mixed-valence double perovskites $Cs_2Au_2X_6$ (X= F, Cl, Br, I), Phys. Lett. 384 (8) (2020) 126169.

[38] U.-G. Jong, C.-J. Yu, Y.-M. Jang, G.-C. Ri, S.-N. Hong, Y.-H. Pae, Revealing the stability and efficiency enhancement in mixed halide perovskites $MAPb(I_{1-x}Cl_x)_3$ with ab initio calculations, J. Power Sources 350 (2017) 65–72.

[39] E. Schreiber, O.L. Anderson, N. Soga, J.F. Bell, Elastic Constants and Their Measurement, 1975.

[40] M. Born, On the stability of crystal lattices. I, Math. Proc. Camb. Phil. Soc. (1940) 160–172.

[41] J. Wang, S. Yip, S.R. Phillpot, D. Wolf, Crystal instabilities at finite strain, Phys. Rev. Lett. 71 (25) (1993) 4182.

[42] D.G. Pettifor, Theoretical predictions of structure and related properties of intermetallics, Mater. Sci. Technol. 8 (4) (1992) 345–349.

[43] X. Luan, H. Qin, F. Liu, Z. Dai, Y. Yi, Q. Li, The mechanical properties and elastic anisotropies of cubic Ni_3Al from first principles calculations, Crystals 8 (8) (2018) 307.

[44] M.E. Fine, L.D. Brown, H.L. Marcus, Elastic constants versus melting temperature in metals, Scripta Metall. 18 (9) (1984) 951–956.

[45] H. Belhadj, et al., Optical properties of $(Pb_{1-x}Mn_xS)_{1-y}Fe_y$ materials from first-principles calculations, Chin. J. Phys. 55 (3) (2017) 1032–1043.

[46] H.A. Eivari, Z. Sohbatzadeh, P. Mele, M.H.N. Assadi, Low thermal conductivity: fundamentals and theoretical aspects in thermoelectric applications, Mater. Today Energy 21 (2021) 100744.

[47] M. Sajjad, Q. Mahmood, N. Singh, J.A. Larsson, Ultralow lattice thermal conductivity in double perovskite Cs_2PtI_6: a promising thermoelectric material, ACS Appl. Energy Mater. 3 (11) (2020) 11293–11299.

[48] T.M. Bhat, D.C. Gupta, Magneto-electronic, thermal, and thermoelectric properties of some Co-based quaternary alloys, J. Phys. Chem. Solid. 112 (2018) 190–199.

[49] F. Tran, P. Blaha, Accurate band gaps of semiconductors and insulators with a semilocal exchange-correlation potential, Phys. Rev. Lett. 102 (22) (2009) 226401.

[50] H. Jiang, Band gaps from the Tran-Blaha modified Becke-Johnson approach: a systematic investigation, J. Chem. Phys. 138 (13) (2013).

[51] P. Borlido, J. Schmidt, A.W. Huran, F. Tran, M.A.L. Marques, S. Botti, Exchange-correlation functionals for band gaps of solids: benchmark, reparametrization and machine learning, npj Comput. Mater. 6 (1) (2020) 96.

[52] S.A. Dar, B. Want, DFT study of structural, mechanical, and opto-electronic properties of scadium-based halide double perovskite $Cs_2ScInBr_6$ for optoelectronic applications, Micro and Nanostructures 170 (2022) 207370.

[53] M. Hassan, I. Arshad, Q. Mahmood, Computational study of electronic, optical and thermoelectric properties of X_3PbO (X= Ca, Sr, Ba) anti-perovskites, Semicond. Sci. Technol. 32 (11) (2017) 115002.

[54] Y. Cai, et al., Computational study of halide perovskite-derived A_2BX_6 inorganic compounds: chemical trends in electronic structure and structural stability, Chem. Mater. 29 (18) (2017) 7740–7749.
[55] A.H. Slavney, T. Hu, A.M. Lindenberg, H.I. Karunadasa, A bismuth-halide double perovskite with long carrier recombination lifetime for photovoltaic applications, J. Am. Chem. Soc. 138 (7) (2016) 2138–2141.
[56] A. El Amrani, et al., Determination of the suitable refractive index of solar cells silicon nitride, Superlattice. Microst. 73 (2014) 224–231, https://doi.org/10.1016/j.spmi.2014.05.025.
[57] J. Sun, H.-T. Wang, J. He, Y. Tian, Ab initio investigations of optical properties of the high-pressure phases of ZnO, Phys. Rev. B 71 (12) (2005) 125132.
[58] D.-Y. Hu, et al., First-principles study on the structural, elastic, electronic and optical properties of lead-free double perovskites Cs_2CuBiX_6 (XI, Br, Cl), Mater. Today Commun. 29 (2021) 102842.
[59] Y. Liu, et al., Hexagonal lead-free Cs_2AgBiI_6 perovskite nanocrystals: a promising material for solar cell application, ACS Appl. Energy Mater. (2023).
[60] T.-Y. Tang, X.-H. Zhao, D.-Y. Hu, Q.-Q. Liang, X.-N. Wei, Y.-L. Tang, An ab-initio investigation of novel double halide perovskite Cs_2InCoX_6 (X= F, Cl, Br) materials with direct band structure and broadband light absorption, Mater. Sci. Semicond. Process. 152 (2022) 107047.
[61] J. Xie, F. Liu, K. Yan, "Chapter 5 - perovskite solar cells processed by solution nanotechnology," in advanced nanomaterials for solar cells and light emitting diodes, in: F. Gao (Ed.), Micro and Nano Technologies, Elsevier, 2019, pp. 119–174, https://doi.org/10.1016/B978-0-12-813647-8.00005-9.
[62] Q. Mahmood, M. Hassan, S.H.A. Ahmad, A. Shahid, A. Laref, Study of optoelectronic and thermoelectric properties of $BaSiO_3$ perovskite under moderate pressure for energy renewable devices applications, J. Phys. Chem. Solid. 120 (2018) 87–95.
[63] M. Houari, et al., Lead-free semiconductors with high absorption: insight into the optical properties of $K_2GeSnBr_6$ and K_2GeSnI_6 halide double perovskites, JETP Lett. 112 (6) (2020) 364–369.
[64] N. Dhar, A. Bandyopadhyay, D. Jana, Tuning electronic, magnetic and optical properties of germanene nanosheet with site dependent adatoms arsenic and gallium: a first principles study, Curr. Appl. Phys. 17 (4) (2017) 573–583.
[65] W. Li, et al., Crystal structure induced ultralow lattice thermal conductivity in thermoelectric Ag_9AlSe_6, Adv. Energy Mater. 8 (18) (2018) 1800030.
[66] M.A. Ali, et al., Appealing perspectives of structural, electronic, mechanical, and thermoelectric properties of $Tl_2(Se, Te)Cl_6$ vacancy-ordered double perovskites, J. Phys. Chem. Solid. 159 (2021) 110258.